One- and two-photon detachment of H^- with excitation of $H(n=2)$

Chih-Ray Liu,* Ning-Yi Du, and Anthony F. Starace
Department of Physics and Astronomy, The University of Nebraska, Lincoln, Nebraska 68588-0111
(Received 13 November 1990)

The cross sections for one- and two-photon detachment of H^- with excitation of the degenerate $H(2s)$ and $H(2p)$ levels are calculated within an adiabatic hyperspherical representation. Both the partial cross sections, $\sigma(2s)$ and $\sigma(2p)$, and the photoelectron angular distribution asymmetry parameters are obtained. Our one-photon detachment results are dominated by the $^1P^o$ shape resonance feature above threshold, which is well known from prior theoretical and experimental work, with which our results are compared in detail. Our two-photon detachment cross sections and angular distribution asymmetry parameters exhibit a half-cycle of dipole-field-induced oscillation in the energy region from the $H(n=2)$ threshold to approximately 34 meV above threshold. The occurrence of a half-cycle of oscillation with significant amplitude over a 34-meV energy region above the $H(n=2)$ threshold is due to two circumstances unique to this two-photon process: first, in contrast to the strongly suppressed oscillations in the $^1S^e$ and $^1P^o$ attractive dipole-field channels for the $H(n=2)$-e^- system, the amplitude of oscillation in the channel having $^1D^e$ symmetry is not strongly suppressed above threshold; second, electric dipole selection rules for the two-photon process do not permit population of the intense $^1P^o$ shape resonance located above the $H(n=2)$ threshold, which would otherwise obscure the half-cycle of dipole-field-induced oscillation. For these reasons, the process of two-photon detachment of H^- is a favorable one for observing this dipole-field-induced oscillation above threshold, which has yet to be observed experimentally in any process.

I. INTRODUCTION

The low-energy states of the fundamental $H(n=2)$-e^- three-body system have been of longstanding theoretical and experimental interest, for two reasons especially. First, the dipole interaction between the detached electron and the degenerate $H(2s)$ and $H(2p)$ energy levels can result in an attractive long-range potential in particular channels.[1] Processes involving transitions to these channels have been shown theoretically to have finite cross sections at threshold, which oscillate above threshold.[2] Second, one of the $^1P^o$ channels of the $H(n=2)$-e^- system has a well-known shape resonance approximately 18 meV above the detachment threshold.[3] The influences of these two effects have been analyzed for a number of processes involving the $H(n=2)$-e^- system: Low-energy electron impact excitation of H has been treated by Gailitis and Damburg[2] and by Macek and Burke,[3(a)] among others. Single-photon detachment of H^- with excitation of H has attracted a number of theoretical studies[3(b),4,5] because this process focuses on the $^1P^o$ shape resonance feature and because electron correlation is essential for its description. Additionally, detailed experimental data for this process have been obtained.[6–8] Lastly, the influences of the long-range attractive dipole field and of the $^1P^o$ shape resonance on fast H^- detachment collisions with rare-gas targets have been analyzed recently by Liu and Starace.[9]

The occurrence of Gailitis-Damburg oscillations[2] has never been observed experimentally above the $H(n=2)$ threshold. Indeed, such oscillations in the total cross section are predicted to be strongly suppressed above threshold.[10,11] Liu and Starace[9(a),9(b)] pointed out that such oscillations are in general not suppressed in differential cross sections, which are sensitive to phase interference effects between different channels. They predicted[9(a)] sizable dipole-field-induced oscillations in the angular distributions for collisional detachment of H^- accompanied by excitation of $H(n=2)$. However, for this process the intense shape resonance feature at 18 meV above threshold in one of the $^1P^o$ final-state channels obscures these oscillations in the meV energy region. These predicted sizable oscillations can only therefore be observed in the collisional detachment process in the experimentally inconvenient energy region below 1 meV above threshold. A major result of this paper is the quantitative prediction of a half-cycle of sizable Gailitis-Damburg cross-section oscillation[2] over an experimentally accessible energy region of tens of meV for the process of two-photon detachment of H^- with excitation of $H(n=2)$.

More specifically, in this paper we employ an adiabatic hyperspherical representation[12] to obtain theoretical results for the one- and two-photon detachment cross sections for H^- with excitation of $H(n=2)$, i.e.,

$$\gamma + H^- \longrightarrow H(n=2) + e^- , \tag{1}$$

$$2\gamma + H^- \longrightarrow H(n=2) + e^- . \tag{2}$$

 ©1991 The American Physical Society

We also obtain the corresponding photoelectron angular distributions. The advantage of photons as probes of the H($n = 2$)-e^- system is that only a few final states, having particular symmetries, are excited. Thus, the photodetachment process (1) involves only $^1P^o$ final states; consequently, the cross section near threshold is dominated by the $^1P^o$ shape resonance. The two-photon detachment process (2), on the other hand, populates only ^1S and ^1D final states due to electric-dipole selection rules; consequently, this process permits a better demonstration of long-range attractive dipole field effects — in particular, of Gailitis-Damburg oscillations[2] — since, in contrast to collisional detachment processes,[2,9(a)] these effects are not obscured by the intense $^1P^o$ shape resonance feature. Indeed, a half-cycle of oscillation in both the $2s$ and $2p$ partial cross sections and in the corresponding angular distributions is shown to be observable over the energy range from 0.5 meV to approximately 34 meV. In the *partial cross sections*, these oscillations are due essentially entirely to an *oscillating amplitude* for transition to one of the $^1D^e$ final-state channels. The magnitude of this oscillation of the transition amplitude is shown to be sizable, in contrast to all other cases that have been considered so far.[10,11] In the *angular distributions*, these oscillations are due primarily to *phase interference effects* similar to those considered in Refs. 9(a) and 9(b), in which the energy dependence of the analytically determined phase shift arising from the long-range dipole field was shown to be rapidly decreasing above threshold.

We have chosen to carry out our calculations in the adiabatic hyperspherical representation because of its utility in describing the states of the H($n = 2$)-e^- system. First, this representation incorporates many of the electron correlations that are important for this system. In particular, Lin[13] has shown that the key Feshbach and shape resonance features of the $^1P^o$ final states may be understood immediately upon observing the structures of the three $^1P^o$ hyperspherical radial potentials for this system. Second, this representation describes correctly at asymptotic separations the effects of the long-range dipole interaction between the degenerate H($2p$) and H($2s$) states and the detached electron; i.e., at large separations this dipole interaction is diagonal in the adiabatic hyperspherical representation.[12,13]

Our results using the adiabatic hyperspherical representation may be summarized briefly as follows. For the photodetachment process (1), our cross sections are in reasonable agreement with the relative experimental data of Bryant and co-workers.[6–8] All theoretical calculations, however, differ significantly from one another in their predictions for the height, width, and energy position of the $^1P^o$ shape resonance feature. Our predicted photoelectron angular distributions, however, are in reasonable agreement with the predictions of Hyman, Jacobs, and Burke.[4] For the two-photon detachment process (2), as already stated, our cross sections demonstrate the occurrence of a half-cycle of significant Gailitis-Damburg oscillation[2] in the experimentally accessible energy region within a few tens of meV of the detachment threshold. These oscillations occur in both the H($2s$) and H($2p$) partial cross sections as well as in the corresponding photoelectron angular distribution asymmetry parameters.

In Sec. II we summarize our theoretical formulation. In Sec. III we present our cross sections and angular distributions for single-photon detachment of H^- with excitation to H(n=2) and make comparisons with experimental and other theoretical results. In Sec. IV we present our cross sections and angular distributions for two-photon detachment of H^- with excitation to H(n=2). In that section we also discuss in some detail the conditions that determine whether the Gailitis-Damburg oscillations[2] will be observable and show that those conditions are favorable for the two-photon process that we consider. Finally, in Sec. V we present our conclusions.

II. THEORETICAL FORMULATION

The wave functions employed in the current calculations have been described in detail in Ref. 9(b). Furthermore, the adiabatic hyperspherical method has been presented in detail by several authors.[12,14–16] Finally, formulas for the calculation of electric dipole transition matrix elements using adiabatic hyperspherical wave functions have been published.[17] In this section, therefore, we present only the key formulas needed to understand our theoretical approach and refer the interested reader to these other references for relevant details.

A. The final-state wave functions

The incoming-wave-normalized wave function describing a final state in which asymptotically the H atom is excited to its nlm level and the detached electron departs with relative momentum $\mathbf{k}$ is

$$\Psi^-_{nlm\mathbf{k}}(\mathbf{r}_1,\mathbf{r}_2) = k^{-1/2}\sum_{l',m'}\sum_{L,M}\sum_{\mu}\Psi^-_{\mu k}(R,\alpha,\hat{\mathbf{r}}_1,\hat{\mathbf{r}}_2)e^{-i\xi_\mu}A^\dagger_{\mu,(ll')}\langle LM|lml'm'\rangle Y^*_{l'm'}(\hat{\mathbf{k}}). \tag{3}$$

Here $\Psi^-_{\mu k}$ is an incoming-wave-normalized hyperspherical wave function for the channel μ; this wave function is dependent on the hyperradius $R \equiv (r_1^2 + r_2^2)^{1/2}$ and the five angular variables $\alpha \equiv \tan^{-1}(r_2/r_1)$, $\hat{\mathbf{r}}_1$, and $\hat{\mathbf{r}}_2$. ξ_μ is an analytically determined phase characteristic of the channel μ. (Both $\Psi^-_{\mu k}$ and ξ_μ are described in more detail below.) The matrix $A^\dagger_{\mu,(ll')}$ transforms the dipole field channels μ to the independent electron channels ll' characterized by the orbital angular momenta l and l' of the H atom electron and the detached electron, respectively. The channel index μ designates implicitly the total orbital and spin angular momenta, LS, of the final

state, although this fact is not made explicit in Eq. (3) for simplicity of notation. Similarly, the dependence of the wave function $\Psi^-_{\mu k}$ on the magnetic quantum numbers M and M_S corresponding to L and S is also suppressed. The Clebsch-Gordan coefficient projects the total orbital angular momentum state $< LM|$ onto the independent electron state $|lml'm' >$, while the spherical harmonic projects the detached electron state $< l'm'|$ onto the state having momentum direction $\hat{\mathbf{k}}$. Lastly, the prefactor k^{-1} in Eq. (3) is needed to ensure normalization of the wave function in Eq. (3) to a δ function in electron momentum $\mathbf{k}$.

1. Adiabatic hyperspherical representation

The incoming-wave-normalized hyperspherical channel wave function $\Psi^-_{\mu k}$ in Eq. (3) is given by

$$\Psi^-_{\mu k}(R,\alpha,\hat{\mathbf{r}}_1,\hat{\mathbf{r}}_2) = (R^{5/2}\cos\alpha\sin\alpha)^{-1}\Phi_\mu(R,\alpha,\hat{\mathbf{r}}_1,\hat{\mathbf{r}}_2)F_{\mu k}(R)e^{-i\eta_\mu} . \tag{4}$$

The prefactor on the right-hand side is a weight factor.[12] Φ_μ is the adiabatic hyperspherical angle function, which is a function of the five angles α, $\hat{\mathbf{r}}_1$, and $\hat{\mathbf{r}}_2$ and is dependent only parametrically on R. It satisfies an angular equation[12,14–16] having eigenvalue $U_\mu(R)$. Here μ labels a particular solution of this angular equation for specified values of total orbital and spin angular momentum. $F_{\mu k}(R)$ is an energy-normalized radial function of R for the μth channel and η_μ is its phase shift, which is defined later below. In general, the radial functions for different channels μ satisfy a set of coupled radial equations;[12,14–16] however, in the adiabatic approximation[12] all but the diagonal coupling matrix elements are dropped so that each $F_{\mu k}(R)$ satisfies a one-dimensional radial Schrödinger equation

$$\left(\frac{d^2}{dR^2} - V_\mu(R) + k^2\right) F_{\mu k}(R) = 0 . \tag{5}$$

In Eq. (5) the effective radial potential $V_\mu(R)$, which characterizes the dynamical features of a particular hyperspherical channel μ converging to the nth level of the H atom, is defined by

$$-V_\mu(R) \equiv \frac{U_\mu(R)+\frac{1}{4}}{R^2} + \left(\Phi_\mu, \frac{d^2\Phi_\mu}{dR^2}\right) - \frac{1}{n^2} , \tag{6}$$

where $(\Phi_\mu, d^2\Phi_\mu/dR^2)$ is the R-dependent diagonal coupling matrix element for the μth channel. Since the long-range dipole interaction due to the degeneracy of the H(n=2) states[1] is diagonal in the hyperspherical representation,[12,13,15] the asymptotic form of the effective radial potential is

$$V_\mu(R) \underset{R\to\infty}{\sim} \lambda_\mu(\lambda_\mu+1)/R^2 . \tag{7}$$

Here λ_μ is an effective orbital angular momentum, which may be real or complex depending on the channel μ. The effective potentials $V_\mu(R)$ that are important for processes (1) and (2) are shown in Fig. 1. Those potentials that converge asymptotically to the H(n=1) level are shown in Fig. 1(a); those that converge to the H(n=2) level are shown in Figs. 1(b) and 1(c). The channels μ in Fig. 1(a) are identified uniquely by their total orbital and spin angular momenta; those in Figs. 1(b) and 1(c) require additional specification. For these latter potentials we employ abbreviated labels corresponding to Lin's classification of doubly excited states.[18] Note finally that the adiabatic $^1P+$ and $^1P-$ curves have a sharply avoided crossing near $R \approx 13.3$ a.u., implying a very strong interaction between them at this value of R. Following others,[12,13,18] we take this strong interaction into account by replacing the adiabatic potentials by the corresponding diabatic potentials (near $R \approx 13.3$ a.u. only) and ignoring any residual interaction between the potentials. We emphasize that this use of the diabatic approximation is limited to these two potentials. All of the six other potentials (as well as $^1P+$ and $^1P-$ potentials outside the $R \approx 13.3$ a.u. region) are calculated by solving the adiabatic hyperspherical equations.

2. Asymptotic forms

The energy-normalized radial wave functions tend asymptotically to

$$F_{\mu k}(R) \underset{R\to\infty}{\sim} (2/\pi k)^{1/2}\sin(kR+\xi_\mu+\eta_\mu) , \tag{8}$$

where η_μ is the phase shift in the μth channel and ξ_μ is an analytically determined phase dependent on the effective angular momentum λ_μ characterizing the long-range dipole interaction of the H($n=2$)-e^- system.[19] *For real values of* λ_μ,

$$\xi_\mu \equiv -\tfrac{1}{2}\pi\lambda_\mu , \tag{9}$$

while *for complex values of* λ_μ, one may write, quite generally,[19]

$$\lambda_\mu = -\tfrac{1}{2} + i\alpha_\mu , \tag{10}$$

in which case[19]

$$\xi_\mu \equiv -\tfrac{1}{4}\pi + \theta_\mu , \tag{11}$$

where

$$\theta_\mu \equiv -\tan^{-1}\frac{\tan[\alpha_\mu\ln(k/2)+x_\mu]}{\tanh(\pi\alpha_\mu/2)} \tag{12}$$

and

$$x_\mu \equiv \arg\Gamma(1-i\alpha_\mu) . \tag{13}$$

The angular functions tend asymptotically to[12]

$$\Phi_\mu(R,\alpha,\hat{\mathbf{r}}_1,\hat{\mathbf{r}}_2) \underset{r_1\to\infty}{\sim} r_1^{1/2}\sum_{l,l'} P_{nl}(r_2)\mathcal{Y}_{ll'LM}(\hat{\mathbf{r}}_2,\hat{\mathbf{r}}_1)A_{(ll'),\mu}\ . \tag{14}$$

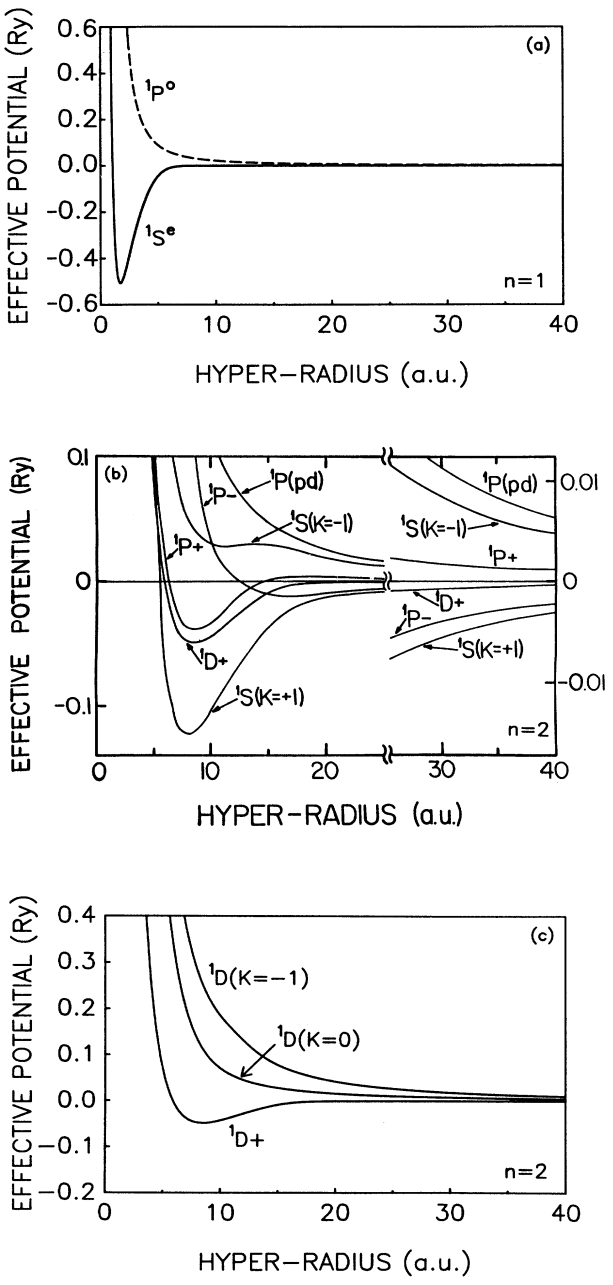

FIG. 1. Effective radial hyperspherical potentials V_μ in Ry plotted vs the hyperradius R. (a) The ^1S and ^1P potentials converging to H($n=1$), which is chosen as the zero of energy. (b) The $^1S(K=\pm1)$, $^1P\pm$, $^1P(pd)$, and $^1D+$ potentials converging to H($n=2$), which is chosen as the zero of energy. Note that in (b) the vertical energy scale is changed at $R=25$. (c) The $^1D+$, $^1D(K=0)$, and $^1D(K=-1)$ potentials converging to H($n=2$); the $^1D+$ is the same one shown in (b).

In Eq. (14), $P_{nl}(r_2)$ is the radial wave function for the nl level of atomic hydrogen and $\mathcal{Y}_{ll'LM}(\hat{\mathbf{r}}_2,\hat{\mathbf{r}}_1)$ is defined by

$$\mathcal{Y}_{ll'LM}(\hat{\mathbf{r}}_2,\hat{\mathbf{r}}_1)\equiv\sum_{m,m'} Y_{lm}(\hat{\mathbf{r}}_2)Y_{l'm'}(\hat{\mathbf{r}}_1)\langle lml'm'|LM\rangle\ . \tag{15}$$

3. Significance of complex λ_μ

The physical significance of a complex value for the effective orbital angular momentum λ_μ [cf. Eq. (10)] is that asymptotically the long-range dipole interaction is attractive. Thus, the effective potential $V_\mu(R)$ at asymptotic radii [cf. Eq. (7)] is negative. As a consequence, the threshold value of the cross section for any excitation to the channel μ is finite[2] since it depends on $|k^{\lambda_\mu+1/2}|^2=1$. In addition, as noted by Gailitis and Damburg,[2] the transition matrix elements for channels having complex λ_μ are influenced above threshold by the term $k^{\lambda_\mu+1/2}=k^{i\alpha_\mu}$ [cf. Eq. (10)], which, when rewritten as $\exp(i\alpha_\mu\ln k)$, may be seen to oscillate as a function of $\ln k$. Of the potentials converging to H(n=2), those labeled $\mu=^1D+$, $^1P-$, and ^1S(K=+1) correspond to complex angular momenta λ_μ. As may be seen in Fig. 1(b), each of these potentials is attractive at large distances R.

B. The initial-state wave function

The initial-state wave function for H^- is given in the adiabatic hyperspherical approximation by

$$\psi_0(\mathbf{r}_1,\mathbf{r}_2)=(R^{5/2}\cos\alpha\sin\alpha)^{-1}\Phi_{\mu=0}(R,\alpha,\hat{\mathbf{r}}_1,\hat{\mathbf{r}}_2)F_{\mu=0}(R), \tag{16}$$

where $\mu=0$ is the lowest adiabatic hyperspherical ^1S channel. The potential for this channel is shown in Fig. 1(a). $\Phi_{\mu=0}$ becomes proportional to the H($1s$) wave function as $r_1\to\infty$. $F_{\mu=0}(R)$ is the lowest-energy radial solution for the μ=0 ^1S potential shown in Fig. 1(a). This wave function has been used in calculations of collisional detachment of H^- by Liu and Starace.[9]

C. The one-photon transition amplitude

For a final-state wave function of the form in Eq. (3) and an initial-state wave function of the form in Eq. (16), the length form of the electric dipole matrix element for the one-photon process (1) for incident light linearly polarized along the z axis is defined by,[17]

$$T^{(1)}_{nlmk} \equiv \left\langle \psi^-_{nlmk} \left| \hat{\epsilon}_z \cdot \sum_{i=1}^{2} \mathbf{r}_i \right| \psi_0 \right\rangle$$
$$= < \psi^-_{nlmk} | R(\cos\alpha \cos\theta_1 + \sin\alpha \cos\theta_2) | \psi_0 >$$
$$= k^{-1/2} \sum_{l',m'} \sum_{L,M} Y_{l'm'}(\hat{\mathbf{k}}) < lml'm' | LM > X^{(1)LM}_{nl,kl'} , \quad (17)$$

where $X^{(1)LM}_{nl,kl'}$ is the amplitude for a one-photon electric dipole transition from the initial state to a final state of angular momentum LM characterized by the hydrogen atom in the nl state and the detached electron having wave number k and orbital angular momentum l'. Specifically,

$$X^{(1)LM}_{nl,kl'} \equiv \sum_{\mu} A_{(ll'),\mu} e^{i(\xi_\mu + \eta_\mu)} \int_0^\infty dR\, F_{\mu k}(R) R F_0(R) I_{\mu 0}(R) , \quad (18)$$

where the result of the angular integrations is given by $I_{\mu 0}(R)$,

$$I_{\mu 0}(R) \equiv \int_0^{\pi/2} d\alpha \int d\Omega_1 \int d\Omega_2 \Phi_\mu(R;\alpha,\hat{\mathbf{r}}_1,\hat{\mathbf{r}}_2)(\cos\alpha\cos\theta_1 + \sin\alpha\cos\theta_2)\Phi_0(R;\alpha,\hat{\mathbf{r}}_1,\hat{\mathbf{r}}_2) . \quad (19)$$

Typically, the hyperspherical angle functions $\Phi_\mu(R;\alpha,\hat{\mathbf{r}}_1,\hat{\mathbf{r}}_2)$ may be expressed as an expansion in coupled spherical harmonics [cf. Eq. (15)]. In this case the integrations over the angles $\hat{\mathbf{r}}_1$ and $\hat{\mathbf{r}}_2$ may be performed analytically. The general result for $I_{\mu 0}(R)$ for the case of linearly polarized light treated in Eq. (19) is given by Eq. (9) of Ref. 17. Other cases of light polarization may of course be obtained from Eq. (19) through use of the Wigner-Eckart theorem. For the specific case of one-photon detachment of the ^1S ground state of H^- by linearly polarized light, the integrations in Eq. (19) give δ functions that restrict the final state to $L = 1$, $M = 0$. We retain the general labels LM on the one-photon transition amplitudes $X^{(1)LM}$, however, in order to emphasize the similarity between the one-photon transition amplitude $T^{(1)}$, in Eq. (17), and the two-photon amplitude $T^{(2)}$, defined in Sec. II D.

D. The two-photon transition amplitude

Two-photon detachment of H^- in which the H atom is unexcited in the final state has been treated in the adiabatic hyperspherical approximation by Fink and Zoller.[20] A general description of multiphoton processes for two-electron systems within the adiabatic hyperspherical representation has been given by Gao, Pan, Liu, and Starace.[21] We treat in this paper the two-photon detachment process (2) in which the H atom is excited to the $n = 2$ level by procedures similar to those of Refs. 20 and 21, which we outline briefly here.

For a final-state wave function of the form in Eq. (3) and an initial-state wave function of the form in Eq. (16), the amplitude for the two-photon process (2) for the case of incident light linearly polarized along the z axis is

$$T^{(2)}_{nlmk} \equiv \left\langle \psi^-_{nlmk} \left| \hat{\epsilon}_z \cdot \sum_{i=1}^{2} \mathbf{r}_i \frac{1}{E_0 + \omega - H} \hat{\epsilon}_z \cdot \sum_{i=1}^{2} \mathbf{r}_i \right| \psi_0 \right\rangle , \quad (20)$$

where E_0 is the ground-state energy, ω is the photon frequency, and H is the atomic Hamiltonian. Defining formally a function

$$|\nu\rangle \equiv \frac{1}{E_0 + \omega - H} \hat{\epsilon}_z \cdot \sum_{i=1}^{2} \mathbf{r}_i |\psi_0\rangle , \quad (21)$$

we expand $|\nu\rangle$ in adiabatic hyperspherical angle functions Φ_μ,

$$|\nu\rangle = (R^{5/2} \sin\alpha\cos\alpha)^{-1} \sum_\mu \nu_\mu(R) \Phi_\mu(R;\alpha,\hat{\mathbf{r}}_1,\hat{\mathbf{r}}_2) , \quad (22)$$

where the coefficients $\nu_\mu(R)$ of this expansion satisfy the following inhomogeneous radial equation

$$\left(k'^2 + \frac{d^2}{dR^2} - V_\mu(R)\right) \nu_\mu(R) = 2R I_{\mu 0}(R) F_0(R) . \quad (23)$$

In Eq. (23), the photoelectron wave number k' is defined by

$$\tfrac{1}{2}k'^2 \equiv E_0 + \omega + \frac{1}{2n^2} , \quad (24)$$

the effective potential $V_\mu(R)$ is defined by Eq. (6), $F_0(R)$ is the radial part of the initial-state wave function [cf. Eq. (16)], and $I_{\mu 0}(R)$ is the angular integral defined in Eq. (19) and evaluated explicitly in Eq. (9) of Ref. 17 for the case of linearly polarized light.

The boundary conditions for the function $\nu_\mu(R)$ have been discussed in detail by Aymar and Crance.[22] For $k'^2 < 0$, $\nu_\mu(R)$ must be finite at both $R = 0$ and $R \to \infty$. For $k'^2 > 0$, $\nu_\mu(R)$ must be finite at $R = 0$ and have no component of the regular solution of the homogeneous equation at $R \to \infty$. The asymptotic boundary condition on $\nu_\mu(R)$ is therefore[22]

$$\nu_\mu(R) \underset{R\to\infty}{\sim} -\frac{\pi}{2}\left(\frac{2}{\pi k'}\right)^{1/2}\cos(k'R+\xi_\mu+\eta_\mu)\,2\int_0^\infty F_\mu(R)RI_{\mu 0}(R)F_0(R)dR\,, \tag{25}$$

where $F_\mu(R)$ is the solution of the homogeneous equation corresponding to Eq. (23), the factor $\pi/2$ represents the Wronskian of the regular and irregular solutions of the homogeneous equation, the function $(2/\pi k')^{1/2}\cos(k'R+\xi_\mu+\eta_\mu)$ is the asymptotic form of the irregular solution of the homogeneous equation, and the radial integral in Eq. (25) gives the electric dipole matrix element between the ground state and the adiabatic hyperspherical channel μ for the total energy $(E_0+\omega)$.

With the solutions $\nu_\mu(R)$ of the radial equations (23) in hand, the two-photon transition amplitude in Eq. (20) may be expressed using Eqs. (3), (4), (21), and (22) as

$$T^{(2)}_{nlm\mathbf{k}} = k^{-1/2}\sum_{l',m'}\sum_{L,M} Y_{l'm'}(\hat{\mathbf{k}})\langle lml'm'|LM\rangle X^{(2)LM}_{nl,kl'}\,, \tag{26}$$

where $X^{(2)LM}_{nl,kl'}$ is the amplitude for a two-photon electric dipole transition from the initial state to a final state of angular momentum LM characterized by the hydrogen atom in the nl state and the detached electron having wave number k and orbital angular momentum l'. Specifically,

$$X^{(2)LM}_{nl,kl'} \equiv \sum_{\mu'} A_{(ll'),\mu'} e^{i(\xi_{\mu'}+\eta_{\mu'})}\Bigg(\sum_\mu \int_0^\infty dR\, F_{\mu' k}(R)RI_{\mu'\mu}(R)\nu_\mu(R) - i\pi\int_0^\infty dR' F_{\mu' k}(R')R' I_{\mu'\mu''}(R')F_{\mu''}(R')\int_0^\infty dR\, F_{\mu''}(R)RI_{\mu''0}(R)F_0(R)\Bigg), \tag{27}$$

where

$$\tfrac{1}{2}k^2 \equiv E_0 + 2\omega + \frac{1}{2n^2}\,, \tag{28}$$

and where the imaginary term inside the large parentheses stems from the standard treatment[23] of the pole in Eq. (20) for the case of the intermediate-state channel $\mu'' \equiv {}^1P^o$ converging to the H($n=1$) threshold. Numerically, the contribution of this latter term as compared to the real term inside the large parentheses is almost negligible for the results we report below.

E. Photoelectron angular distributions

The transition amplitudes for processes (1) and (2) in Eqs. (17) and (26), respectively, have the same structure. Hence the angular distributions may be calculated for both processes using the following general formula for $q = 1, 2$ (where q is the photon number):

$$\sum_m \left|T^{(q)}_{nlm\mathbf{k}}\right|^2 = k^{-1}\sum_m \sum_{\substack{l',m'\\ l'',m''}}\sum_{\substack{L',M'\\ L,M}} (X^{(q)L'M'}_{nl,kl''})^\dagger \langle L'M'|lml''m''\rangle Y^*_{l''m''}(\hat{\mathbf{k}})Y_{l'm'}(\hat{\mathbf{k}})\langle lml'm'|LM\rangle X^{(q)LM}_{nl,kl'}\,. \tag{29}$$

Using well-known relations for expressing the product of spherical harmonics as an expansion in single spherical harmonics,[24] summing over the magnetic quantum numbers m, m', and m'' using a well-known relation for $3j$ symbols,[25] and noting that for the spherically symmetric initial states with which we are concerned here, $M = M'$ is fixed by the polarization of the incident light, we obtain

$$\sum_m |T^{(q)}_{nlm\mathbf{k}}|^2 = (4\pi k)^{-1}\sum_{l',l''}\sum_{L,L'} (X^{(q)L'M}_{nl,kl''})^\dagger X^{(q)LM}_{nl,kl'}(-1)^{L-M+l'} \times \sum_\lambda [\lambda]([l'][l''][L][L'])^{1/2}\begin{pmatrix}\lambda & l' & l''\\ 0 & 0 & 0\end{pmatrix}\begin{pmatrix}\lambda & L & L'\\ 0 & -M & M\end{pmatrix}\begin{Bmatrix}\lambda & L & L'\\ l & l'' & l'\end{Bmatrix} P_\lambda(\cos\theta_{\hat{\mathbf{k}}})\,. \tag{30}$$

In Eq. (30), $\theta_{\hat{\mathbf{k}}}$ is measured with respect to the axis of linear polarization in the case of linearly polarized incident light and with respect to the incident light beam in the case of circularly polarized light. The symbol $[x]$ denotes $2x+1$.

III. RESULTS FOR SINGLE-PHOTON DETACHMENT

The single-photon detachment process (1) in which the H atom is excited to the H(n=2) level has been studied

both experimentally[6–8] and theoretically.[3(b),4,5] Its theoretical description requires detailed consideration of electron correlations since this process cannot be described by an independent electron model. Comparison of our results with those of these other studies provides an indication of the accuracy of the adiabatic hyperspherical approximation's description of electron correlation effects. Such an indication is important for judging our predictions for the corresponding two-photon process (2), presented in Sec. IV, since there are no experimental or other theoretical results for this process of which we are aware.

A. Cross-section formulas

Single-photon detachment of the $^1S^e$ ground state of H^- leads only to $^1P^o$ final states. The differential cross sections for the H(2s) and H(2p) states are given by

$$\frac{d\sigma_{2l}}{d\Omega} = 4\pi^2\omega\alpha k \sum_m \left|T^{(1)}_{2lmk}\right|^2 , \tag{31}$$

which, using Eq. (30), may be written for the case of linearly polarized incident light as follows:

$$\frac{d\sigma_{2l}}{d\Omega} = \frac{\sigma_{2l}}{4\pi}[1 + \beta_{2l}P_2(\cos\theta_{\hat{\mathbf{k}}})] , \tag{32}$$

where

$$\sigma_{2l} = 4\pi^2\omega\alpha \sum_{l'} |X_{2l,kl'}|^2 \quad \text{for } l = 0,1, \tag{33}$$

$$\beta_{2s} = 2 , \tag{34}$$

$$\beta_{2p} = \frac{4\pi^2\omega\alpha}{\sigma_{2p}}[|X_{2p,kd}|^2 - 2^{1/2}(X^\dagger_{2p,ks}X_{2p,kd} + X_{2p,ks}X^\dagger_{2p,kd})] . \tag{35}$$

In these equations, $X_{2l,kl'}$ is given by Eq. (18) with $L = 1$, $M = 0$. The differential cross section for the case of circularly polarized incident light is simply related to Eq. (32): $+\beta_{2l}$ in Eq. (32) is replaced by $-\beta_{2l}/2$ and $\theta_{\hat{\mathbf{k}}}$ is measured with respect to the direction of the incident light.[26]

B. Calculational details

The effective potentials for the adiabatic hyperspherical channels μ over which the sum is performed in Eq. (18) are presented in Fig. 1(b). There are three $^1P^o$ potentials, indicated by $^1P+$, $^1P-$, and $^1P(pd)$. [As noted in Sec. II A 1 above, near $R \approx 13.3$ the adiabatic $^1P+$ and $^1P-$ potentials have been replaced by the corresponding diabatic potentials.] As discussed in detail by Lin,[13] the $^1P+$ potential is attractive at short distances and weakly repulsive at large distances thereby giving rise to a shape resonance at about 18 meV above threshold. The $^1P(pd)$ potential is strongly repulsive at all distances. Finally, the $^1P-$ potential is repulsive only at short distances, but is attractive at large distances. This channel has a complex effective angular momentum λ_μ, and, as discussed in Sec. II A 3, gives rise to a small but finite cross section at threshold. However, due to the shape resonance near-threshold, Gailitis-Damburg oscillations[2] near threshold are obscured. In addition, Gailitis-Damburg oscillations are extremely weak for the $^1P-$ channel.[11,27] For these reasons, we do not examine the near-threshold behavior of the cross section in detail for this process.

Our results for the radially dependent angular integrals $I_{\mu 0}(R)$, defined in Eq. (19), are shown in Fig. 2 for the three ^1P final-state channels μ relevant for process (1). We see that these three angular integrals have significant and comparable amplitudes at both small and large radii R. This is to be contrasted with the radial functions, $F_\mu(R)$, which have very different amplitudes, at small R in particular, as may be deduced from the corresponding effective potentials shown in Fig. 1(b).

C. Results

Our results for the total $n = 2$ cross section, i.e., $\sigma_{2s}+\sigma_{2p}$, are shown in Fig. 3 in comparison with the relative experimental data of Butterfield.[8] As pointed out by Lin,[13] the hyperspherical potential $^1P+$ predicts a shape resonance about 18.9 meV too high. In order to compare our $n = 2$ cross sections with experiment, we have therefore shifted our curves 18.9 meV lower in energy *for this figure only.* The experimental data in Fig. 23 of Ref. 8 have a nonzero background below threshold; we have subtracted this background from the data above threshold. Furthermore, we have normalized the experimental data to our theoretical prediction at the peak of the shape resonance. As shown in Fig. 3, our theoretically predicted $n = 2$ cross section is somewhat wider in energy than that measured experimentally. Nevertheless, the agreement is quite reasonable considering that our final-state hyperspherical potentials are uncoupled.

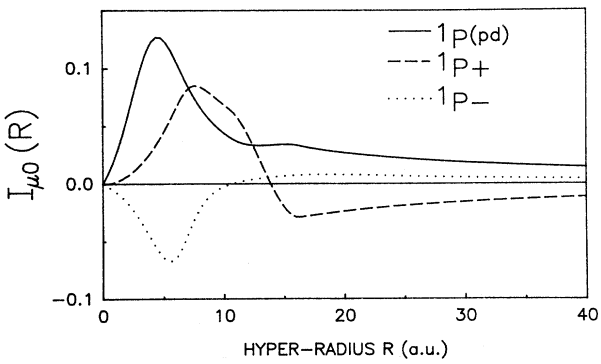

FIG. 2. Radial dependence of the angular integrals $I_{\mu 0}(R)$ defined in Eq. (19) for the three $^1P^o$ hyperspherical channels $\mu =$ $^1P+$, $^1P-$, and $^1P(pd)$.

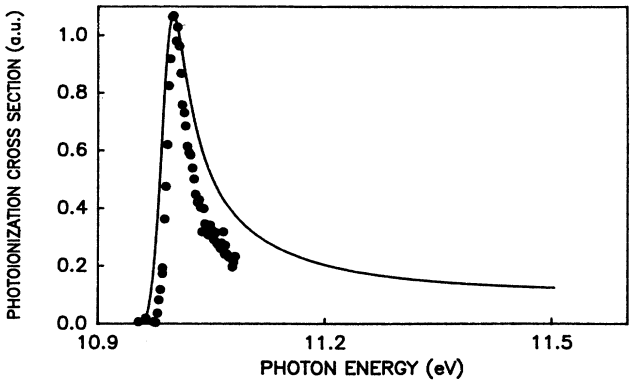

FIG. 3. Photodetachment cross section for the process $\gamma + H^- \longrightarrow H(n = 2) + e^-$. Solid line: present (dipole length) adiabatic hyperspherical results, shifted to the experimental peak position. Solid circles: relative experimental data of Butterfield (Ref. 8) normalized to our predicted peak height.

Figure 4 compares our theoretical results for the total $n = 2$ cross section with predictions of Hyman, Jacobs, and Burke[4] and Broad and Reinhardt.[5] (Macek's results[3(b)] for the $n = 2$ cross section are only given explicitly for photon energies considerably higher than those shown in Fig. 4.) The $1s$-$2s$-$2p$ close-coupling calculation of Hyman, Jacobs, and Burke[4] gives the lowest, broadest, and highest energy prediction for the shape resonance feature. The 160 configuration J-matrix calculation of Broad and Reinhardt[5] gives the highest, narrowest, and lowest energy prediction for the shape resonance feature. The present hyperspherical results for the height, width, and position of the shape resonance feature are intermediate between the results of these two other calculations. The relative experimental results[7] for the *total* H^- detachment cross section in the neighborhood of

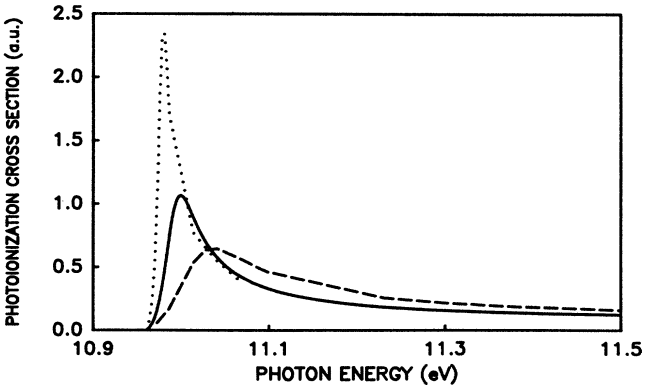

FIG. 4. Theoretical (dipole length) predictions for the photodetachment cross section for the process $\gamma + H^- \longrightarrow H(n = 2) + e^-$. Solid line: present adiabatic hyperspherical results. Dashed line: $1s$-$2s$-$2p$ close-coupling results of Hyman, Jacobs, and Burke (cf. Table 1 of Ref. 4). Dotted line: 160 configuration J-matrix results of Broad and Reinhardt (cf. Fig. 6 of Ref. 5).

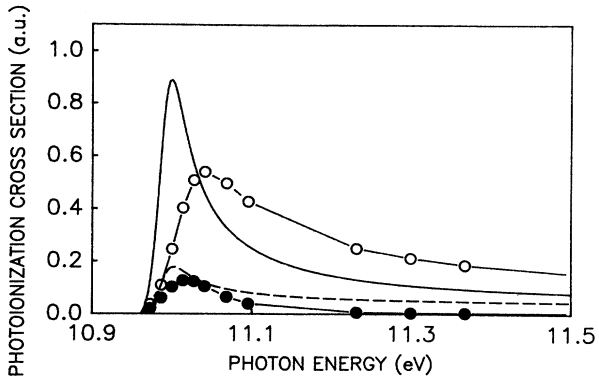

FIG. 5. Theoretical (dipole length) predictions for the partial photodetachment cross sections $\sigma(2s)$ and $\sigma(2p)$ for the process $\gamma + H^- \longrightarrow H(2s, 2p) + e^-$. Solid [dashed] lines: present adiabatic hyperspherical results for $\sigma(2p)$ [$\sigma(2s)$]. Open [closed] circles: $1s$-$2s$-$2p$ close-coupling results of Hyman, Jacobs, and Burke for $\sigma(2p)$ [$\sigma(2s)$] (cf. Table 1 of Ref. 4).

the $n = 2$ threshold have been fitted in detail to the corresponding theoretical results of Broad and Reinhardt[5] taking into account the experimental resolution. Very good agreement was obtained.[7] Nevertheless, the sensitivity of the theoretical calculations for the $n = 2$ cross section to the approximations employed, as demonstrated in Fig. 4, indicates a need for an absolute experimental measurement of the $n = 2$ cross section.

In Fig. 5 we present our results for the partial cross sections for detaching H^- and leaving the H atom in the $2s$ and $2p$ states. We compare our dipole length results with the corresponding dipole length results of Hyman, Jacobs, and Burke.[4] Our results agree qualitatively with those of Hyman, Jacobs, and Burke. In particular, both calculations predict that $\sigma(2p)$ is significantly larger than $\sigma(2s)$ in the vicinity of the $n = 2$ detachment threshold. As far as we are aware, there are no other theoretical re-

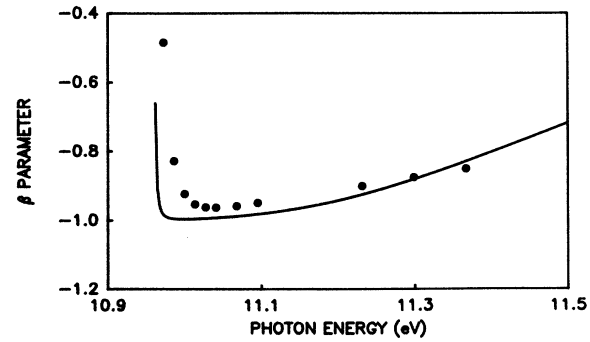

FIG. 6. Theoretical (dipole length) predictions for the photoelectron angular distribution asymmetry parameter, β_{2p} [cf. Eq. (35)], for the process $\gamma + H^- \longrightarrow H(2p) + e^-$. Solid line: present adiabatic hyperspherical results. Solid circles: $1s$-$2s$-$2p$ close-coupling results of Hyman, Jacobs, and Burke (cf. Table 1 of Ref. 4).

sults for these partial cross sections with which to compare.

Finally, in Fig. 6 we present our results for the angular distribution asymmetry parameter for the H($2p$) final state. This asymmetry parameter β_{2p} is defined in Eq. (35). Once again we compare our dipole length results with the only other theoretical results of which we are aware, namely, those of Hyman, Jacobs, and Burke.[4] The two predictions are in very good agreement.

IV. RESULTS FOR TWO-PHOTON DETACHMENT

Experimental observation of nonresonant multiphoton detachment of H^- ions has recently been reported.[28] In anticipation of future, more refined experimental measurements, we present here theoretical predictions for process (2) in which two photons detach H^- and excite the $n = 2$ level of the H atom. A key feature of our results for this two-photon detachment process is the presence of a half-cycle of Gailitis-Damburg oscillation[2] in the cross sections above the H($n = 2$) threshold over an energy region of tens of meV.

A. Cross-section formulas

Two-photon detachment of the $^1S^e$ ground state of H^- leads only to $^1S^e$ and $^1D^e$ final states in the case of linearly polarized photons and only to $^1D^e$ final states in the case of circularly polarized photons. The differential cross sections for the H($2s$) and H($2p$) states are given by

$$\frac{d\sigma_{2l}}{d\Omega} = 8\pi^3\alpha^2\omega^2 k \sum_m \left| T^{(2)}_{2lm\mathbf{k}} \right|^2 , \tag{36}$$

which, using Eq. (30), may be written as

$$\frac{d\sigma_{2l}}{d\Omega} = \frac{\sigma_{2l}}{4\pi} \sum_{j=0}^{2} \beta^{2l}_{2j} P_{2j}(\cos\theta_{\hat{\mathbf{k}}}) . \tag{37}$$

For the case of *linearly polarized incident light*, the partial cross sections σ_{2l} and the asymmetry parameters β^{2l}_{2j} ($j = 0, 1, 2$) are defined in terms of the two-photon transition amplitudes $X^{(2)LM}_{2l,kl'}$ in Eq. (27) as follows:

$$\sigma_{2s} = 8\pi^3\alpha^2\omega^2(|X^{(2)00}_{2s,ks}|^2 + |X^{(2)20}_{2s,kd}|^2), \tag{38}$$

$$\beta^{2s}_0 = 1, \tag{39}$$

$$\beta^{2s}_2 = \frac{8\pi^3\alpha^2\omega^2}{\sigma_{2s}} \{\tfrac{10}{7}|X^{(2)20}_{2s,kd}|^2 + 5^{1/2} \times 2\,\mathrm{Re}[(X^{(2)20}_{2s,kd})^\dagger X^{(2)00}_{2s,ks}]\}, \tag{40}$$

$$\beta^{2s}_4 = \frac{8\pi^3\alpha^2\omega^2}{\sigma_{2s}} \frac{18}{7} \left| X^{(2)20}_{2s,kd} \right|^2 , \tag{41}$$

$$\sigma_{2p} = 8\pi^3\alpha^2\omega^2(|X^{(2)00}_{2p,kp}|^2 + |X^{(2)20}_{2p,kp}|^2 + |X^{(2)20}_{2p,kf}|^2), \tag{42}$$

$$\beta^{2p}_0 = 1, \tag{43}$$

$$\beta^{2p}_2 = \frac{8\pi^3\alpha^2\omega^2}{\sigma_{2p}} \left[|X^{(2)20}_{2p,kp}|^2 + \tfrac{8}{7}|X^{(2)20}_{2p,kf}|^2 + 2\,\mathrm{Re}\left(-2^{1/2}(X^{(2)00}_{2p,kp})^\dagger X^{(2)20}_{2p,kp} + 3^{1/2}(X^{(2)00}_{2p,kp})^\dagger X^{(2)20}_{2p,kf} - \frac{6^{1/2}}{7}(X^{(2)20}_{2p,kp})^\dagger X^{(2)20}_{2p,kf} \right) \right], \tag{44}$$

$$\beta^{2p}_4 = \frac{8\pi^3\alpha^2\omega^2}{\sigma_{2p}} \left(\frac{6}{7}|X^{(2)20}_{2p,kf}|^2 - \frac{6^{3/2}}{7} \times 2\,\mathrm{Re}[(X^{(2)20}_{2p,kp})^\dagger X^{(2)20}_{2p,kf}] \right) . \tag{45}$$

For the case of *circularly polarized incident light*, the corresponding partial cross sections and asymmetry parameters are given by

$$\sigma_{2s} = 8\pi^3\alpha^2\omega^2|X^{(2)22}_{2s,kd}|^2, \tag{46}$$

$$\beta^{2s}_0 = 1, \tag{47}$$

$$\beta_2^{2s} = -10/7, \tag{48}$$

$$\beta_4^{2s} = +3/7, \tag{49}$$

$$\sigma_{2p} = 8\pi^3\alpha^2\omega^2(|X_{2p,kp}^{(2)22}|^2 + |X_{2p,kf}^{(2)22}|^2), \tag{50}$$

$$\beta_0^{2p} = 1, \tag{51}$$

$$\beta_2^{2p} = \frac{8\pi^3\alpha^2\omega^2}{\sigma_{2p}}\left(-|X_{2p,kp}^{(2)22}|^2 - \frac{8}{7}|X_{2p,kf}^{(2)22}|^2 + \frac{6^{1/2}}{7} \times 2\,\mathrm{Re}[(X_{2p,kp}^{(2)22})^\dagger X_{2p,kf}^{(2)22}]\right), \tag{52}$$

$$\beta_4^{2p} = \frac{8\pi^3\alpha^2\omega^2}{\sigma_{2p}}\left(\frac{1}{7}|X_{2p,kf}^{(2)22}|^2 - \frac{6^{1/2}}{7} \times 2\,\mathrm{Re}[(X_{2p,kp}^{(2)22})^\dagger X_{2p,kf}^{(2)22}]\right). \tag{53}$$

In the above equations, Re[a] denotes the real part of the complex number a.

B. Calculational details

The effective $^1P^o$ potentials $V_\mu(R)$, which determine in part the solutions $\nu_\mu(R)$ in Eq. (23), are shown in Fig. 1. The $^1P^o$ potential converging asymptotically to H($1s$) is shown in Fig. 1(a); those converging to H(n=2) are shown in Fig. 1(b) and have already been discussed in Sec. III B above. The effective $^1S^e$ and $^1D^e$ potentials for the adiabatic hyperspherical channels μ' over which the sum is performed in Eq. (27) are shown in Figs. 1(b) and 1(c). The $^1S(K=-1)$, $^1D(K=0)$, and $^1D(K=-1)$ potentials are strongly repulsive at all distances. On the other hand, the $^1S(K=+1)$ and the $^1D+$ potentials are both attractive and have complex effective angular momenta, λ_μ. As discussed in Sec. II A 3, these channels have small but finite cross sections at threshold. Furthermore, they both exhibit Gailitis-Damburg oscillations[2] near threshold.

C. Observation of dipole-field-induced oscillations

There are two ways in which an attractive dipole field introduces oscillations in measured cross sections on a $\ln k$ energy scale. The first is due to the rapid variation of the analytically determined dipole phase θ_μ [cf. Eqs. (11) and (12)] for those hyperspherical channels μ having complex values of the effective angular momentum λ_μ [cf. Eq. (10)]. This analytically determined phase θ_μ (through ξ_μ) appears explicitly in the phase factor included in the two-photon transition amplitudes $X_{nl,kl'}^{(2)LM}$ in Eq. (27). Interference effects between different amplitudes, such as occur commonly in the angular distribution asymmetry parameters [cf. Eqs. (40), (44), (45), (52), and (53)], generally lead to sizable, undamped oscillations in the corresponding cross sections due to the rapid decrease of the analytically determined phases θ_μ with increasing $\ln k$. This analytic behavior is shown in Fig. 10 of Ref. 9(b).

The second way the long-range dipole field introduces oscillations in the cross sections is through the effective normalization of the final-state wave function for the H(n=2)-e^- system. These additional oscillations may be extracted using generalized quantum defect theory by representing our adiabatic hyperspherical radial wave functions as[29]

$$F_{\mu k}(R) = N_\mu(k)F_{\mu k}^o(R), \tag{54}$$

where $N_\mu(k)$ is the analytically determined effective normalization factor, which determines essentially all of the energy dependence of the radial wave function near $R \approx 0$, and where $F_{\mu k}^o(R)$ is a more smoothly varying function of k. The oscillatory, energy-dependent normalization factor $N_\mu(k)$ is defined as follows:[29]

$$N_\mu(k) = [\, B_\mu \cos^2\eta_\mu + B_\mu^{-1}(1+\mathcal{G}_\mu^2)\sin^2\eta_\mu - \mathcal{G}_\mu \sin 2\eta_\mu]^{1/2}\,, \tag{55}$$

where η_μ is the phase shift in the μth channel [cf. Eq. (8)] and where B_μ and $\mathcal{G}_\mu$ are analytic functions defined by[19]

$$B_\mu = \frac{\sinh \pi\alpha_\mu}{\cosh \pi\alpha_\mu - \cos 2[\alpha_\mu \ln(k/2) + x_\mu]}\,, \tag{56}$$

$$\mathcal{G}_\mu = \frac{-\sin 2[\alpha_\mu \ln(k/2) + x_\mu]}{\cosh \pi\alpha_\mu - \cos 2[\alpha_\mu \ln(k/2) + x_\mu]}\,. \tag{57}$$

The parameters α_μ and x_μ are defined in Eqs. (10) and (13).

As noted by Greene and Rau,[11] the energy dependence of $N_\mu^2(k)$ stems primarily from the function B_μ. In particular, the oscillation amplitude of $N_\mu^2(k)$ is governed primarily by that of B_μ. Now, neglecting terms of order $\exp(-2\pi\alpha_\mu)$ compared to 1, B_μ in Eq. (56) may be approximated by[30]

$$B_\mu \approx [1 - 2e^{-\pi\alpha_\mu}\cos 2(\alpha_\mu \ln(k/2) + x_\mu)]^{-1}\,. \tag{58}$$

TABLE I. Dipole potential strengths $[\lambda_\mu(\lambda_\mu+1)]$, complex parts of λ_μ (α_μ), and oscillatory damping factors $(2e^{-\pi\alpha_\mu})$ for the $^1S^e$, $^1P^o$, and $^1D^e$ attractive dipole potentials of the $H(n=2)-e^-$ system.

Term (^1L)	$\lambda_\mu(\lambda_\mu+1)$ [a]	α_μ [b]	$2e^{-\pi\alpha_\mu}$
$^1S^e$	−5.0827	2.198	0.20×10^{-2}
$^1P^o$	−3.7082	1.860	0.58×10^{-2}
$^1D^e$	−0.8102	0.748	19.08×10^{-2}

[a] From Refs. 1 and 2, $\lambda_\mu(\lambda_\mu+1)=L^2+L+1-[(2L+1)^2+36]^2$.
[b] From Eq. (10), $\alpha_\mu=[-\lambda_\mu(\lambda_\mu+1)-1/4]^{1/2}$.

Hence, one sees clearly that the amplitude factor $2e^{-\pi\alpha_\mu}$ for the oscillatory cosine term is in general likely to be small. This suppression of the dipole-field-induced oscillations above threshold was first pointed out by Fabrikant[10] and was analyzed in detail for single-photon photodetachment of H^- with excitation of the residual H atom by Greene and Rau.[11] However, as we show in Table I, the $^1D^e$ channel of the $H(n=2)$-e^- system is only very weakly damped due to its having an unusually small value of α_μ. Consequently, in contrast to the $^1S^e$ and $^1P^o$ attractive dipole channels, whose oscillations have amplitudes of 0.2% and 0.6%, respectively, the $^1D^e$ channel has an amplitude of oscillation of 19%. Explicit calculations[9(b)] of the normalization factors $N_\mu(k)$ for these three channels confirmed these predictions, as shown in Fig. 11 of Ref. 9(b). For this reason, the two-photon detachment process (2) is a very favorable one for observing dipole-field-induced oscillations above threshold, particularly since the intense (and nonoscillatory) $^1P^o$ shape resonance channel, which would obscure the effect, is not populated.

D. Results

Our results for the two-photon detachment cross sections σ_{2s} and σ_{2p} as well as the total cross section for the $n=2$ subshell, $\sigma_{2s}+\sigma_{2p}$, are shown in Fig. 7 plotted versus $\ln k$ so that the Gailitis-Damburg oscillations above threshold can be seen clearly. Conversion of $\ln k$ to photoelectron energy above the $H(n=2)$ threshold is given in Table II. As indicated in Table II, the assumption of degeneracy in the $n=2$ level of H breaks down due to the spin-orbit interaction and the Lamb shift at values of $\ln k \lesssim -6$. We have nevertheless plotted our results over the region $\ln k \geq -9$ in order to exhibit two cycles of the oscillatory behavior expected above threshold under the assumption that the $n=2$ levels are degenerate.

Figure 7(a) shows our results for the case of linearly (L) polarized light using Eqs. (38) and (42); Fig. 7(b) shows our results for the case of circularly (C) polarized light using Eqs. (46) and (50). In the region of $\ln k \gtrsim -3$, the oscillatory behavior of the cross sections becomes irregular and arises not only from Gailitis-Damburg oscillations but also from dynamical oscillations stemming from, e.g., the free-free matrix elements, which determine the two-photon amplitude in Eq. (27). This amplitude involves an overlap of the final-state radial function $F_{\mu' k}(R)$ with the continuum radial function $\nu_\mu(R)$ defined by Eqs. (23)–(25). In order to disentangle these other dynamical effects from the Gailitis-Damburg oscillations, we plot renormalized cross sections for the cases of linearly polarized and circularly polarized incident light in Figs. 7(c) and 7(d), respectively. The renormalized cross sections are obtained by dividing all transition amplitudes by the effective normalization factor $N_\mu(k)$ discussed in Sec. IV C above and defined by Eqs. (54) and (55). These normalization factors contain the oscillatory behavior expected to arise from the long-range dipole field. As is seen clearly in Figs. 7(c) and 7(d), removal of the energy dependence embodied in these normalization factors results in constant cross sections in the region $-9 \leq \ln k \lesssim -3$. The remaining energy dependence of these renormalized cross sections shown in Figs. 7(c) and 7(d) in the region $\ln k \gtrsim -3$ is due to other dynamical effects.

We conclude therefore that the region $-6 \lesssim \ln k \lesssim -3$ is the energy region in which the long-range dipole field interaction determines the energy behavior of the cross sections. This region lies between the energy region $\ln k \lesssim -6$ at which the assumption of energy-level degeneracy breaks down and the energy region $\ln k \gtrsim -3$ in which other dynamical influences have significant effects. This region encompasses more than a half cycle of oscillation of the cross sections, including a minimum at $\ln k \approx -5$ and a succeeding sharp rise in the cross sections to a maximum at $\ln k \approx -2.8$.

Plots of our cross section results, shown in Figs. 7(a) and 7(b) on a $\ln k$ scale, are given on an energy scale in Fig. 8. Figures 8(a) and 8(b) give our results for the case of linearly (L) polarized light and Figs. 8(c) and 8(d) give our results for the case of circularly (C) polarized light. Figures 8(a) and 8(c) present the energy region from 0.025 – 25 meV, over which essentially the entire energy dependence is due to the half-cycle of the Gailitis-Damburg oscillation shown in Figs. 7(a) and 7(b) over the region $-6 \lesssim \ln k \lesssim -3$. One sees that there are minima near 0.5 meV [located in Figs. 7(a) and 7(b) at $\ln k \approx -5$] and significant 30% and 50% rises in the linear and circular polarization cross sections respectively over the energy range up to 25 meV. The cross-section maxima appearing at $\ln k \approx -2.8$ in Figs. 7(a) and 7(b) occur in Figs. 8(b) and 8(d) as the peaks near 0.05 eV. The cross sections shown in these figures over the energy region up to 5 eV above threshold reflect many dynamical influences and not just long-range dipole field effects, as explained above in our discussion of the renormalized cross sections in Figs. 7(c) and 7(d).

The angular distribution asymmetry parameters, β_2 and β_4, are shown in Fig. 9 for the cases of both linearly and circularly polarized light. Those for the $2s$ subshell of H are defined by Eqs. (40), (41), (48), and (49) and those for the $2p$ subshell are defined by Eqs. (44), (45), (52), and (53). In addition, we have plotted the asymme-

try parameters for the H($n = 2$) subshell; these average asymmetry parameters are defined by [cf. Eq. (37)]:

$$\beta_{2j}^{n=2} \equiv \frac{\sigma_{2s}\beta_{2j}^{2s} + \sigma_{2p}\beta_{2j}^{2p}}{\sigma_{2s} + \sigma_{2p}} \qquad (j = 1, 2) \,. \tag{59}$$

One sees that many of these asymmetry parameters also have strongly oscillatory behavior above the $n = 2$ threshold. As discussed in Sec. IV C, this oscillatory behavior may be understood in terms of two effects of the long-range dipole field: the oscillatory behavior of the effective normalization factor, $N_\mu(k)$, and the rapid energy variation of the analytically determined dipole phase shifts ξ_μ and θ_μ [cf. Eqs. (11) and (12)]. In the case of linearly polarized light, β_4^{2s} is determined by the absolute square of a single transition amplitude [cf. Eq(41)]. Its energy dependence is therefore governed essentially entirely by the squared normalization factor $N_\mu^2(k)$ for the $\mu = {}^1D+$ hyperspherical channel, which gives the dominant contribution to this transition amplitude. Its dependence on the analytically determined phase, ξ_μ, is removed when taking the absolute square of this amplitude. This dominance of the $\mu = {}^1D+$ channel over the other two ${}^1D$ final channels explains also why the energy dependence of the asymmetry parameter β_4^{2p} in the case of linearly polarized light and both β_2^{2p} and β_4^{2p} in the case of circularly polarized light are determined primarily by the squared normalization factor $N_\mu^2(k)$ for this dominant hyperspherical channel and not by any phase interference effects. The asymmetry parameters β_2^{2s} and β_2^{2p} for the case of linearly polarized incident light, however, both involve an interference between ${}^1S$ and ${}^1D$ final-state transition amplitudes. For these two cases, the rapid energy variation of the analytically determined phases ξ_μ and θ_μ for the ${}^1S(K = +1)$ and ${}^1D+$ final-state channels may be shown to govern nearly all of the energy dependence in the region $\ln k \lesssim -3$. The remaining weak energy dependence of these two asymmetry parameters may be described analytically using the quantum-defect theory (QDT) for a long-range dipole field to introduce smooth short-range parameters.[11,29] The result of such a QDT analysis is that the remaining energy dependence is determined about equally by the oscillatory normalization factors $N_\mu(k)$ and by the very weak oscillations[31] of the short-range phase shift, η_μ, for the ${}^1D+$ final state. For details of the requisite QDT analysis, the interested reader is referred elsewhere.[11,29]

To summarize this discussion of Fig. 9, we point out

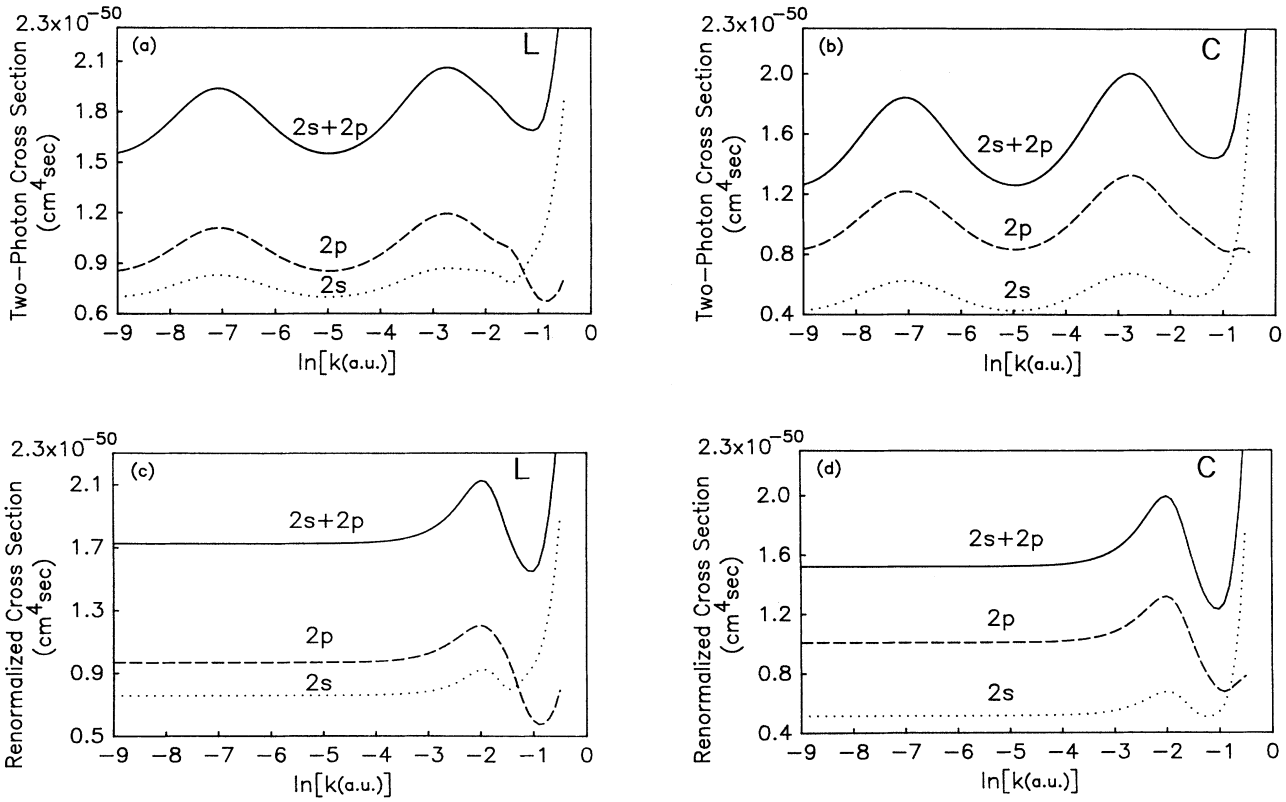

FIG. 7. Generalized two-photon cross sections for the cases of linearly (L) and circularly (C) polarized light for the process $2\gamma + \mathrm{H}^- \longrightarrow \mathrm{H}(2s, 2p) + e^-$ plotted vs $\ln k$, where k (a.u.) is the photoelectron momentum. (a) L results, (b) C results, (c) renormalized L results, and (d) renormalized C results. See text for definition of renormalized cross-section results.

TABLE II. Comparison of $\ln k$ versus electron energy $k^2/2$.

$\ln[k$ (a.u.)]	$k^2/2$ (eV)
−9.0	2.1×10^{-7}
−8.0	1.5×10^{-6}
−7.5	4.3×10^{-6}[a]
−7.0	1.1×10^{-5}
−6.3	4.5×10^{-5}[b]
−6.0	8.4×10^{-5}
−5.0	6.2×10^{-4}
−4.0	4.6×10^{-3}
−3.0	3.4×10^{-2}
−2.0	2.5×10^{-1}
−1.0	1.8
−0.5	5.0

[a]Magnitude of $2s_{1/2}$-$2p_{1/2}$ Lamb shift.
[b]Magnitude of $2p_{1/2}$-$2p_{3/2}$ spin-orbit splitting.

that for the case of linearly polarized light the energy dependence of the asymmetry parameters β_2 and β_4 are measures of two different aspects of the long-range dipole field. Namely, the energy dependences of the β_2 parameters in Fig. 9(a) in the region $-6 \lesssim \ln k \lesssim -3$ are measures of interference between the rapidly varying and analytically determined dipole field phase shifts, θ_μ, defined by Eq. (12), for the $^1S(K = +1)$ and $^1D+$ final-state channels. The energy dependences of the β_4 parameters in Fig. 9(b) in the energy region $-6 \lesssim \ln k \lesssim -3$, on the other hand, are measures of the effective normalization constant $N_\mu(k)$, defined by Eq. (55), for the $^1D+$ channel. As shown in Figs. 9(c) and 9(d), use of circularly polarized light, which populates only the ^1D final-state channels, results in essentially no energy dependence of the β_2 and β_4 parameters in the energy region $-6 \lesssim \ln k \lesssim -3$ in which dipole field effects are expected to be prevalent.

Finally, in Fig. 10 we present our results for the total $n = 2$ differential cross section, which is the sum of the differential cross sections for the $2s$ and $2p$ states defined by Eq. (37). Results are given for the six angles, $\theta_{\hat{\mathbf{k}}} = 0°, 18°, 36°, 54.7°, 72°$, and 90°. [Note that the results labeled $\theta_{\hat{\mathbf{k}}} = 54.7°$ are actually calculated for $\theta_{\hat{\mathbf{k}}} = 54.7356°$, at which $P_2(\theta_{\hat{k}}) = 0$.] One sees from this figure that the energy dependence of the differential cross section in the region $-6 \lesssim \ln k \lesssim -3$ (over which long-range dipole field effects play the major role) is highly dependent on the angle $\theta_{\hat{\mathbf{k}}}$ at which the photoelectron is detected. This energy dependence may be enhanced by

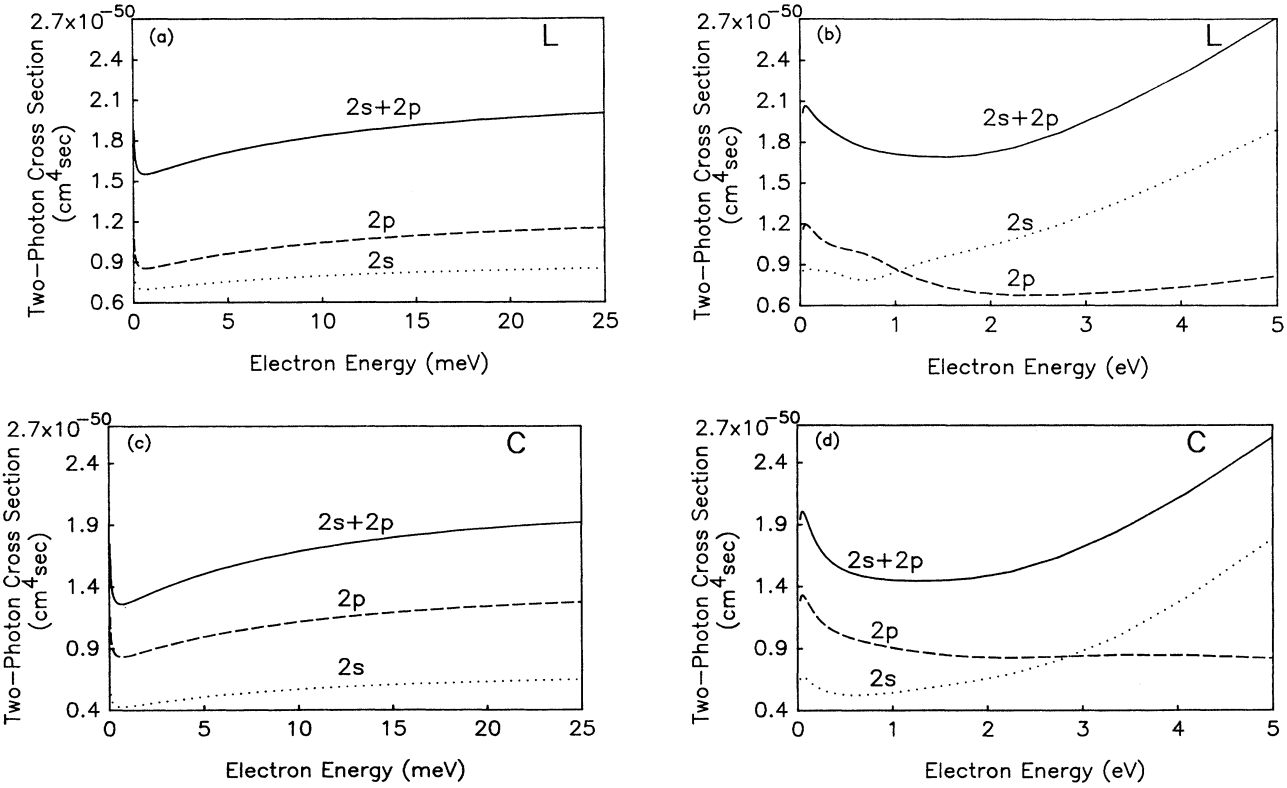

FIG. 8. Generalized two-photon cross sections for the cases of linearly (L) and circularly (C) polarized light for the process $2\gamma + H^- \longrightarrow H(2s, 2p) + e^-$ plotted vs photoelectron energy. (a) L results on a meV energy scale, (b) L results on an eV energy scale, (c) C results on a meV energy scale, and (d) C results on an eV energy scale. The energy dependences shown in (a) and (c) are due to long-range dipole field effects and originate from a half-cycle of Gailitis-Damburg oscillation.

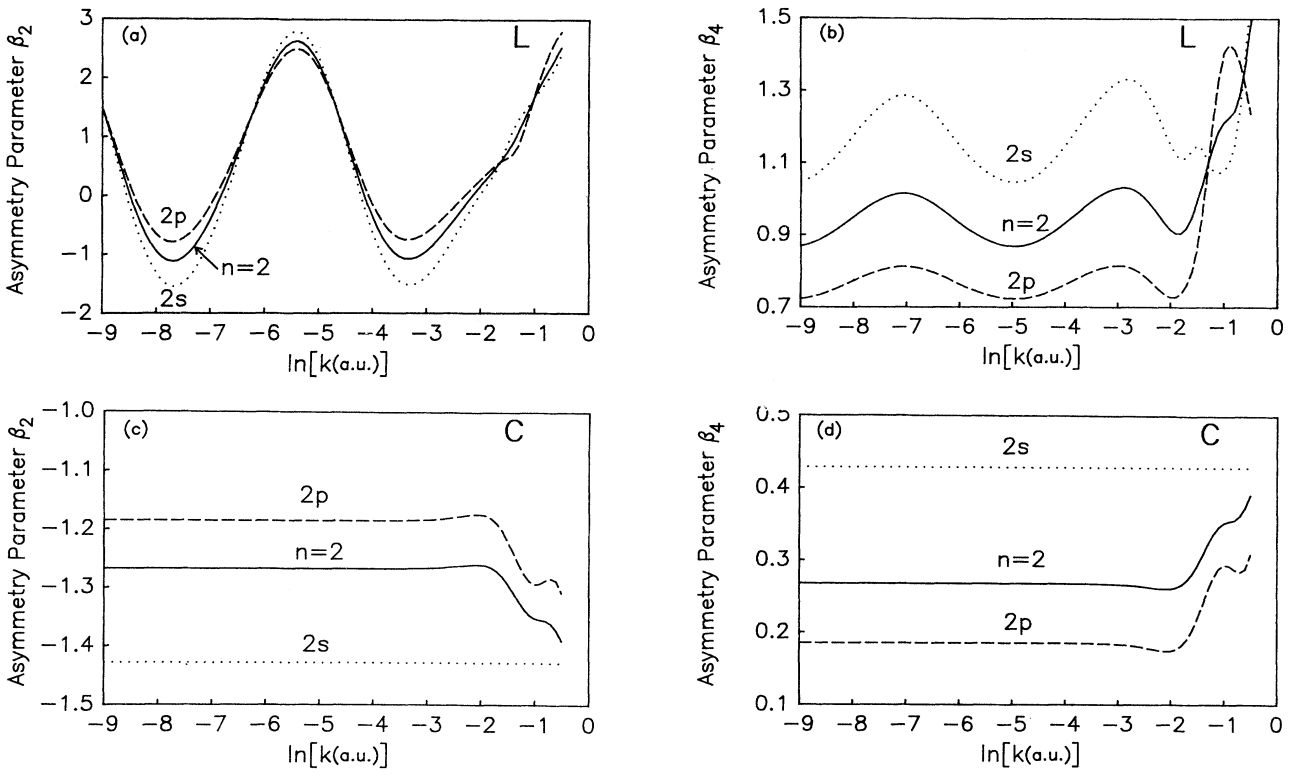

FIG. 9. Photoelectron angular distribution asymmetry parameters for the cases of linearly (L) and circularly (C) polarized light for the process $2\gamma + H^- \longrightarrow H(2s, 2p) + e^-$ plotted vs $\ln k$, where k (a.u.) is the photoelectron momentum. (a) L results for β_2^{2s}, β_2^{2p}, and $\beta_2^{n=2}$ [cf. Eqs. (40), (44), and (59)]; (b) L results for β_4^{2s}, β_4^{2p}, and $\beta_4^{n=2}$ [cf. Eqs. (41), (45), and (59)]; (c) C results for β_2^{2s}, β_2^{2p}, and $\beta_2^{n=2}$ [cf. Eqs. (48), (52), and (59)]; (d) C results for β_4^{2s}, β_4^{2p}, and $\beta_4^{n=2}$ [cf. Eqs. (49), (53), and (59)].

use of linearly polarized light and small angles of detection, $\theta_{\hat{\mathbf{k}}}$.

V. CONCLUSIONS

In this paper we have reported our results using an adiabatic hyperspherical representation for the one- and two-photon detachment of H^- with excitation of the degenerate H(2s) and H(2p) states. As is well known from previous work, the one-photon detachment process is dominated by the $^1P^o$ shape resonance near threshold. Furthermore, its theoretical description requires inclusion of electron correlations. Detailed comparisons of our results are made in Sec. III C with the relative experimental measurements of Butterfield[8] for the total $H(n = 2)$ cross section, with the theoretical results of

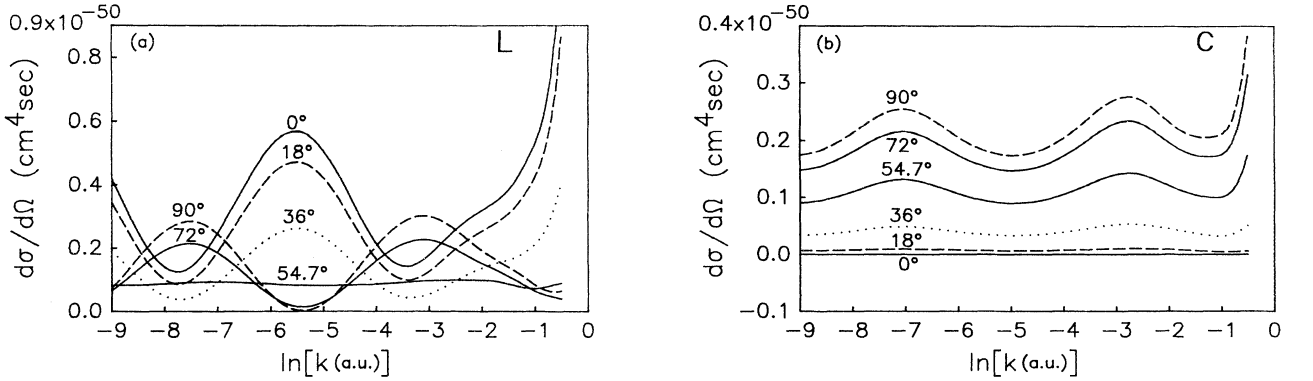

FIG. 10. Differential cross sections [cf. Eq. (37)] for the cases of linearly (L) and circularly (C) polarized light for the process $2\gamma + H^- \longrightarrow H(n = 2) + e^-$ plotted vs $\ln k$, where k (a.u.) is the photoelectron momentum, for the detached electron angles $\theta_{\hat{\mathbf{k}}} = 0°, 18°, 36°, 54.7356°, 72°$, and 90°. (a) L results; (b) C results.

Broad and Reinhardt[5] for the total $H(n = 2)$ cross section, and with the theoretical results of Hyman, Jacobs, and Burke[4] for the $H(2s)$ and $H(2p)$ partial cross sections as well as the corresponding detached electron angular distributions. These comparisons indicate a need for absolute experimental results for each of the $H(2s)$ and $H(2p)$ partial cross sections.

Our results for the two-photon detachment of H^- indicate that long-range dipole field effects dominate the energy dependence of the cross section over the experimentally observable energy region from about 0.5 meV to approximately 34 meV above threshold. In particular, this energy region encompasses more than a half-cycle of Gailitis-Damburg[2] oscillations, which have yet to be observed experimentally. Extensive discussion has been presented in Secs. IV C and IV D of the reasons why this two-photon process in H^- is probably the most likely one in which to observe such effects of long-range dipole fields.

ACKNOWLEDGMENTS

C.R.L. and A.F.S. gratefully acknowledge discussions and correspondence with Howard C. Bryant and Kenneth B. Butterfield concerning details of their experimental data on single-photon detachment of H^-. N.Y.D. gratefully acknowledges discussions with Chris H. Greene concerning QDT for long-range dipole fields. This work was supported in part by the U.S. Department of Energy, Office of Basic Energy Sciences, Division of Chemical Sciences, under Grant No. DE-FG02-88ER13955.

*Present address: Department of Radiation Oncology and Nuclear Medicine, Thomas Jefferson University Hospital, Philadelphia, PA 19107-5097.

[1] M. J. Seaton, Proc. Phys. Soc. London **77**, 174 (1961).

[2] M. Gailitis and R. Damburg, Zh. Eksp. Teor. Fiz. **44**, 1644 (1963) [Sov. Phys.—JETP **17**, 1107 (1963)]; Proc. Phys. Soc. London **82**, 192 (1963); M. Gailitis, in *Atomic Physics 6*, edited by R. Damburg and O. Kukaine (Plenum, New York, 1978), pp. 249–266.

[3] (a) J. Macek and P. G. Burke, Proc. Phys. Soc. **92**, 351 (1967); (b) J. Macek, *ibid.* **92**, 365 (1967).

[4] H. A. Hyman, V. L. Jacobs, and P. G. Burke, J. Phys. B **5**, 2282 (1972).

[5] J. T. Broad and W. P. Reinhardt, Phys. Rev. A **14**, 2159 (1976).

[6] H. C. Bryant, B. D. Dieterle, J. Donahue, H. Sharifian, H. Tootoonchi, D. M. Wolfe, P. A. M. Gram, and M. A. Yates-Williams, Phys. Rev. Lett. **38**, 228 (1977).

[7] H. C. Bryant, D. A. Clark, K. B. Butterfield, C. A. Frost, H. Sharifian, H. Tootoonchi, J. B. Donahue, P. A. M. Gram, M. E. Hamm, R. W. Hamm, J. C. Pratt, M. A. Yates, and W. W. Smith, Phys. Rev. A **27**, 2889 (1983), Sec. VII.

[8] Kenneth B. Butterfield, Ph.D. thesis, The University of New Mexico (1984), Sec. IV. Tabulated data for the $n = 2$ cross section in Fig. 23 appear on pp. 124 and 125.

[9] (a) C. R. Liu and A. F. Starace, Phys. Rev. Lett. **62**, 407 (1989); (b) Phys. Rev. A **40**, 4926 (1989); (c) **42**, 2684 (1990).

[10] I. I. Fabrikant, Zh. Eksp. Teor. Fiz. **73**, 1317 (1977) [Sov. Phys.—JETP **46**, 693 (1977)].

[11] C. H. Greene and A. R. P. Rau, Phys. Rev. A **32**, 1352 (1985).

[12] J. H. Macek, J. Phys. B **1**, 831 (1968).

[13] C. D. Lin, Phys. Rev. Lett. **35**, 1150 (1975).

[14] U. Fano, Rep. Prog. Phys. **46**, 97 (1983).

[15] C. D. Lin, Adv. At. Mol. Phys. **22**, 77 (1986).

[16] A. F. Starace, in *Fundamental Processes of Atomic Dynamics*, edited by J. S. Briggs, H. Kleinpoppen, and H. O. Lutz (Plenum, New York, 1988), pp. 235–258.

[17] C. H. Park, A. F. Starace, J. Tan, and C. D. Lin, Phys. Rev. A **33**, 1000 (1986).

[18] C. D. Lin, Phys. Rev. A **29**, 1019 (1984). See also Ref. 15 above. Specifically, our channels μ converging to the $H(n = 2)$ level have the following labels in Lin's $(K,T)^A$ notation: $^1S(K = \pm 1)$, $(\pm 1, 0)^+$; $^1P+$, $(0,1)^+$; $^1P-$, $(1,0)^-$; $^1P(pd)$, $(-1,0)^0$; $^1D+$, $(1,0)^+$; $^1D(K = 0)$, $(0,1)^0$; $^1D(K = -1)$, $(-1,0)^0$.

[19] C. Greene, U. Fano, and G. Strinati, Phys. Rev. A **19**, 1485 (1979). Note that we take θ_μ in the same quadrant as $-\alpha_\mu \ln \frac{1}{2}k - x_\mu$.

[20] M. G. J. Fink and P. Zoller, J. Phys. B **18**, L373 (1985).

[21] B. Gao, C. Pan, C. R. Liu, and A. F. Starace, J. Opt. Soc. Am. **7**, 622 (1990).

[22] M. Aymar and M. Crance, J. Phys. B **13**, 2527 (1980); **14**, 3585 (1981), Appendix 2.

[23] L. S. Rodberg and R. M. Thaler, *Introduction to the Quantum Theory of Scattering* (Academic, New York, 1967), p.177.

[24] A. R. Edmonds, *Angular Momentum in Quantum Mechanics*, 2nd ed. (Princeton University Press, Princeton, NJ, 1974), Eq. (4.6.5).

[25] A. P. Yutsis, I. B. Levinson, and V. V. Vanagas, *Theory of Angular Momentum* (Israel Program for Scientific Translations, Jerusalem, 1962), Eq. (A.7.4).

[26] See, e.g., S. T. Manson and A. F. Starace, Rev. Mod. Phys. **54**, 389 (1982), Sec. II.

[27] See Fig. 11(b) of Ref. 9(b).

[28] C. Y. Tang, P. G. Harris, A. H. Mohagheghi, H. C. Bryant, C. R. Quick, J. B. Donahue, R. A. Reeder, S. Cohen, W. W. Smith, and J. E. Stewart, Phys. Rev. A **39**, 6068 (1989).

[29] U. Fano and A. R. P. Rau, *Atomic Collisions and Spectra* (Academic, New York, 1986), Secs. 5.4 and 5.7.3.

[30] Note that our result in Eq. (58) differs from the result in Eq. (11) of Ref. 11 due to different definitions of the functions B_μ. These different definitions stem from the different normalization conventions employed in Refs. 19 and 29. We have followed the normalization conventions in Ref. 19; Ref. 11 follows the normalization conventions in Ref. 29, which were originally developed in the paper by C. H. Greene, A. R. P. Rau, and U. Fano, Phys. Rev. A **26**, 2441 (1982).

[31] This weak oscillatory behavior of the $\mu = {}^1D+$ final-state short-range phase shift, η_μ, may be understood as follows. From examination of Eq. (12) for the analytically determined phases, θ_μ, one sees that for large values of α_μ, $\tanh(\pi\alpha_\mu/2) \approx 1$ and thus θ_μ is a linear function of $\ln k$.

This relation holds for the ${}^1S(K = +1)$ and the ${}^1P-$ final-state channels, but not for the ${}^1D+$ final state, which has an unusually small value of α_μ (cf. Table I), giving $\tanh(\pi\alpha_\mu/2) \approx 0.826$. This introduces a slight oscillatory behavior in the energy dependence of θ_μ for $\mu = {}^1D+$ (instead of a strict proportionality to $\ln k$), which may be seen (barely) in Fig. 10 of Ref. 9(b). This in turn leads to a weak oscillatory behavior in the ${}^1D+$ channel's short-range phase shift, η_μ, which is calculated with respect to the long-range dipole phase, θ_μ. It is possible to describe even this residual dipole-field-induced energy dependence of the short-range phase shift, η_μ, by expressing it in terms of the analytic dipole-field functions B_μ and $\mathcal{G}_\mu$ [cf. Eqs. (56) and (57)] and a smooth (i.e., relatively energy independent) short-range phase shift, η_μ^0. This representation is described in Refs. 11 and 29. We have not done this analysis here since our results for the cross sections and angular distribution asymmetry parameters are, of course, independent of the representation used.